



Synchronous generation of H₂O₂ and high effective removal of inorganic arsenic/organoarsenic by visible light-driven cell

Yan Sun, Lei Zhang*

College of Chemistry, Liaoning University, 66 Chongshan Middle Road, Shenyang, Liaoning 110036, People's Republic of China

ARTICLE INFO

Keywords:

Janus electrode
Hydrogen peroxide production
Arsenic contamination remediation
PEC in-situ Fenton system

ABSTRACT

A Janus photocathode of asymmetric wettability with hydrophobic oxygen storage layer and hydrophilic catalyst layer was successfully fabricated by graphite felt (GF) polytetrafluoroethylene (PTFE)-hydrophobization and a subsequent hollow sphere NiFe₂O₄@ZnFe₂O₄ (NF@ZF) Z-scheme photocatalysts coating on the other side of GF. The designed Janus electrode showed significantly higher H₂O₂ production than hydrophilic (NF@ZF/GF) and hydrophobic (NF@ZF/PTFE/GF) electrodes, and achieved a higher faradaic efficiency of 72%, as well as a record H₂O₂ production rate of 255.9 mg·L⁻¹·h⁻¹, while maintaining a stable photoelectrochemical performance for 9 h at 2.8 mA·cm⁻² in Na₂SO₄ solution. The two-electrode co-photoelectrolysis system by coupling the ORR with inorganic arsenic/organoarsenic oxidation can simultaneously produce H₂O₂ at Janus photocathode and As (V) at Fe anode under a low energy consumption (a cell voltage of only 0.7 V), respectively, and then the generated As (V) could be rapidly removed (above 93%) by adsorption onto Fe (III) (hydro)oxides.

1. Introduction

Inorganic arsenic and organoarsenic compounds pose serious health risks to humans, especially in aquatic environments and drinking water. The existence of inorganic arsenic is mainly in two kinds of states such as As (V) and As (III), among them, As (III) is more toxic, more mobile, and less adsorbed on absorbents than As (V) [1]. Therefore, the pre-oxidation of As (III) to As (V) is a desirable step in water pollution treatment. Organoarsenic compounds, take roxarsone (ROX) as an example, have been used intensively as feed additives in poultry and swine production worldwide for several decades. Although ROX has relatively low toxicity, it can be degraded to form the highly toxic As (III) and As (V) through biotic and abiotic transformation, increasing arsenic pollution risk to the ecosystem and environment [2]. Therefore, it is necessary to explore an efficient and eco-friendly strategy for the remediation of arsenic pollution and the simultaneous removal of produced inorganic arsenic species.

Photoelectrochemical (PEC) production and in-situ activation of H₂O₂ for highly efficient oxidation of As (III) and ROX is a promising method to solve problems regarding the arsenic contamination of drinking water. In two-electron oxygen reduction reaction (ORR), sluggish oxygen mass transfer and limited solubility in electrolyte could not provide adequate O₂ supply to hydrophilic catalyst surface, resulting

in a finite performance of the ORR reacting mostly at the electrode/electrolyte interface with only the dissolved oxygen [3]. Researchers proposed that the solid-liquid-gas triple-phase interfaces is essential for ORR performance improvement [4,5]. The superhydrophobic electrode with a triple-phase interfaces greatly improved the internal oxygen diffusion coefficient about 5.7 times compared with the normal gas diffusion electrodes (GDE), bring about the increasement of O₂ utilization efficiency (OUE) (44.5–64.9%), H₂O₂ generation (101.7 mg·h⁻¹·cm⁻²) and Faraday efficiency (66.8%) [6]. However, the surface gas film of the hydrophobic electrodes might result in heavy bubble covering the electrodes, causing serious reduction in catalysts active sites, and blocking the electrode/electrolyte contact. Therefore, how to design a rational and effective electrode for accelerating O₂ transport and keeping fast ion transportation are thought to be a critical challenge in achieving highly efficient PEC ORR.

Janus electrode with asymmetrical wettability on two sides have attracted interest of researchers for their potential applications in ORR. Li et al. designed a Janus cathode exhibited a improved current density of 22.5 mA·cm⁻² compared with the hydrophobic (11.2 mA·cm⁻²) and hydrophilic (3.3 mA·cm⁻²) competitors in the ORR [7]. Zhang et al. engineered a Janus cathode with opposite wetting properties by coating oxidized carbon black and polyvinylidene fluoride (PVDF) on one side of polytetrafluoroethylene (PTFE)-hydrophobized graphite felt [8]. With

* Corresponding author.

E-mail address: zhanglei63@126.com (L. Zhang).

<https://doi.org/10.1016/j.apcatb.2023.123549>

Received 24 September 2023; Received in revised form 14 November 2023; Accepted 20 November 2023

Available online 23 November 2023

0926-3373/© 2023 Elsevier B.V. All rights reserved.

the merits of sufficient oxygen supply from hydrophobic oxygen storage layer and adequate active sites in hydrophilic catalyst layer, the OUE and H_2O_2 production rate of Janus cathode was significantly improved than the hydrophobic or hydrophilic electrodes, enabling more eco-friendly and cost-effective PEC ORR processes. In the Janus electrode, the hydrophobic layer maintains stable oxygen storage to provide abundant oxygen supply, while the hydrophilic catalyst layer guarantees adequate active sites for solution contact, thus the catalysts in the hydrophilic layer could get oxygen with shortening transport distance from hydrophobic side than the external O_2 supply as well as abundant electrolyte percolation.

Among potential catalysts for hydrogen peroxide production, CoO [9], NiFe_2O_4 [10], ZnFe_2O_4 [11] and MnFe_2O_4 [12] are promising photo-electrocatalysts due to their relatively narrow band gap, controllable morphology, and low cost. Furthermore, Z-scheme heterojunction constructed by integrating two different semiconductors with interleaved energy band positions and Fermi energy level positions is supposed to facilitate carrier separation while maintaining the strong redox capability of the constituent semiconductors [10,11,13,14]. At the same time, we are soberly aware that there are still several important problems awaiting solution - how to maximize the utilization of solar and electric energy for high rate H_2O_2 production and continuous generate $\bullet\text{OH}$ by photo-electro-Fenton process for pollutants treatment [15–17].

In this work, in order to accelerate O_2 mass transfer and improve OUE, a Janus electrode with opposite wetting properties for 2e^- ORR was fabricated by modifying hydrophobic PTFE on one side of the 3D porous GF (hydrophobic side), followed by coating self-constructed hollow sphere Z-scheme NiFe_2O_4 @ ZnFe_2O_4 (NF@ZF) photocatalyst on the other side of the GF (hydrophilic side), the Janus electrode maintaining steady oxygen storage in the hydrophobic side while guaranteeing excellent ionic/electronic conductivity in the hydrophilic side. For win-win goals, the photoelectricity-driven cathodic H_2O_2 generation system coupled with Fe as the sacrificial anode realized H_2O_2 production and ROX degradation (or As (III) pre-oxidation) simultaneously via a PEC cell of Janus || Fe with a lower cell voltage. A high production rate (up to $255.9 \text{ mg}\cdot\text{L}^{-1}\cdot\text{h}^{-1}$) of H_2O_2 was achieved by the PEC system, and then the in-situ generated H_2O_2 served as the Fenton reagent for the oxidation of organic and inorganic arsenic. The released As (V) with reduced toxicity then adsorbed rapidly onto iron (hydro)oxide precipitates for the complete removal of arsenic due to the clever use of Fe as the anode by controlling the pH of the electrolyte. The developed Janus || Fe in-situ Fenton system acts as an efficient, sustainable, and eco-friendly approach for generation and in-situ activation of H_2O_2 , which provide a novel strategy for the practical application of advanced oxidation technology in the field of wastewater treatment.

2. Experimental section

2.1. Synthesis of various catalysts

2.1.1. Preparation of hollow spherical NiFe_2O_4

The hollow spherical NiFe_2O_4 (NF) was synthesized by a facile hydrothermal process. Briefly, a homogenous solution of $\text{Ni}(\text{NO}_3)_2\cdot 6\text{H}_2\text{O}$ (0.25 mmol), NH_4F (18 mmol), urea (36 mmol) $\text{Fe}(\text{NO}_3)_3\cdot 9\text{H}_2\text{O}$ (0.5 mmol) and 40 mL deionized water was heated in a Teflon-lined autoclave for 6 h at 180°C . Subsequently, the product was obtained by centrifugation, washing with deionized water and ethanol for three times and then dried at 60°C for 6 h.

2.1.2. Preparation of NiFe_2O_4 @ ZnFe_2O_4 composite

Typically, 0.40 mmol $\text{Fe}(\text{NO}_3)_3\cdot 9\text{H}_2\text{O}$ and 0.20 mmol $\text{Zn}(\text{NO}_3)_2\cdot 6\text{H}_2\text{O}$ dissolved in 50 mL deionized water and 0.2 g of as-prepared NF was added. Then the suspensions were ultrasonicated for 20 min. Subsequently, 800 mg NaOH were added into the mixture and keep stirring for 2 h. Finally, the mixture was transferred into stainless steel autoclave

and kept at 180°C for 12 h. The final products were named as NF@ZF.

2.2. Fabrication of Janus electrode with an opposite wetting properties

6% PTFE solution was modified on one side of the 3D GF substrate ($2 \text{ cm} \times 2 \text{ cm}$), and the electrode was dried under the infrared lamp. During the drying, the PTFE solution could naturally infiltrate the mesh channel by capillary forces and form a hydrophobicity gradient. Then the electrode was annealed at 350°C for 30 min in a furnace. Hydrophilic catalyst was the mixture of 5 mg carbon black (CB), 10 mg NF@ZF and 0.5 mL 8% PVDF/DMF, and then evenly coated on the graphite felt. Finally, the coated graphite felt was dried naturally to obtain the Janus electrode.

For comparison, the hydrophilic electrode (HIE) and hydrophobic electrode (HOE) were also be prepared, and corresponding steps involved were detailed in [Supporting Information](#).

2.3. PEC H_2O_2 production from the photocathode

PEC production of H_2O_2 was conducted in an electrolytic cell of a three-electrode system with the Janus electrode, Pt plate and Ag/AgCl as photocathode, counter electrode and reference electrode, respectively. 20 mL 0.1 M Na_2SO_4 aqueous solution (adjust pH to 3 with $1 \text{ mol}\cdot\text{L}^{-1}$ HClO_4 [18,19]) was used as electrolyte. Before PEC ORR, electrolyte was saturated by O_2 , and the O_2 was continued sparged in solution during the reaction. The photocathode was illuminated under a 300 W Xenon lamp fixed at $100 \text{ mW}\cdot\text{cm}^{-2}$ with a cutoff filter ($\lambda > 420 \text{ nm}$). K_2TiO (C_2O_4)₂ was used as chromogenic agent to measure the concentration of H_2O_2 by UV-vis spectrophotometer [8,20]. [Fig. S1](#) shows the correlation curve of H_2O_2 concentration and absorbance.

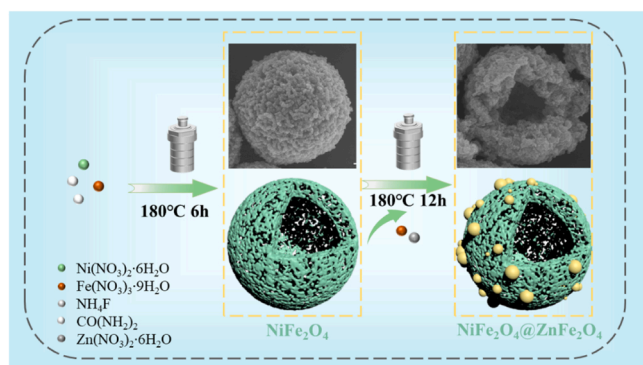
2.4. PEC in-situ Fenton treatment of Arsenic contamination

A single compartment glass cell was chosen to carry out the experiments, which applying the prepared Janus electrode, Ag/AgCl and Fe plate as photocathode, reference electrode and counter electrode, respectively. 20 mL aqueous Na_2SO_4 (0.1 M) solution containing As (III) (20 ppm) or ROX (10 ppm) was used as a supporting electrolyte (pH = 3) under O_2 purge. The photocathode was illuminated under a 300 W Xenon lamp fixed at $100 \text{ mW}\cdot\text{cm}^{-2}$ with a cutoff filter ($\lambda > 420 \text{ nm}$). The concentration of As (V) was measured with molybdenum blue method by UV/Vis spectrophotometer [21,22] and the total As was obtained by potassium permanganate oxidizing. The concentration of As (III) was calculated by deducting the As (V) from total As.

3. Results and discussion

3.1. Characterization of the prepared hydrophilic catalysts

The synthesis route of the hollow spherical NiFe_2O_4 @ ZnFe_2O_4 (NF@ZF) is illustrated in [Scheme 1](#). The microstructures and morphologies of catalysts are observed by scanning electron microscopy (SEM). The synthesized NF with uniform diameter of about 3–4 μm exhibited hollow spherical structure ([Fig. 1a](#)). After loading ZnFe_2O_4 (ZF), the NF@ZF maintain the hollow sphere shape of NiFe_2O_4 (NF) with a more compact outer surface, where the open gap and cavity of composites can be clearly seen, according to the broken sphere as showed [Fig. 1b](#). The void spaces of NF@ZF microspheres were key reasons to increase not only the surface area and active sites but also the ability of light scattering and O_2 uptake. The Energy dispersive X-ray spectrometer (EDS) (inset of [Fig. 1b](#)) and SEM EDS mapping ([Fig. S2](#)) further exhibit the presence of Ni, Zn, Fe and O suggesting that the ZF nanoparticles covers on surface of NF hollow sphere. The X-ray diffraction (XRD) pattern ([Fig. 1c](#)) demonstrated the successful synthesis of the catalysts. The X-ray photoelectron spectroscopy (XPS) of Ni 2p, Zn 2p, Fe 2p and O 1s were exhibited in [Fig. 1d-g](#). Notably, the shift in binding energies in Ni



Scheme 1. Illustration of the synthetic process of hollow spherical $\text{NiFe}_2\text{O}_4 @ \text{ZnFe}_2\text{O}_4$.

and Zn of NF@ZF compared to pure NF and ZF are observed (Fig. 1d, e). These shifts demonstrating the variation of electron density around the atoms and a strong electronic interaction with the electron transfer from NF to ZF in the NF@ZF heterojunction, which is favorable for building Z-scheme heterojunction. In the Fe 2p spectrum of NF and NF@ZF (Fig. 1f), two distinct peaks centered at 724.67 and 711.26 eV correspond to $\text{Fe } 2p_{1/2}$ and $\text{Fe } 2p_{3/2}$, indicating that the Fe element exists in the Fe^{3+} ions. The O 1s spectrum of NF@ZF in Fig. 1g could be divided into three peaks of 529.47, 531.36 and 533.00 eV, which could be

attribute to metal-oxygen bonds, the surface hydroxyl group, and the adsorbed oxygen, respectively. Furthermore, a negative shift in the peaks of NF@ZF compared to NF and ZF can be noted, revealing the NF@ZF heterojunction interactions were achieved via the O atom bridging the Ni of NF and the Zn of ZF to form strongly coupled interface (Ni-O-Zn). The constructed Ni-O-Zn interface could effectively reduce interface contact resistance, facilitate charge transfer, accelerate separation and migration of charge carrier, and thus significantly improve photoelectrocatalytic activities. XPS survey spectrum (Fig. S3) further showed successful synthesis of the NF@ZF.

To investigate the light absorption properties of as-synthesized NF, ZF and NF@ZF catalysts, the UV-vis diffuse reflectance spectra (DRS) were recorded and shown in Fig. S4a, and the band gap of NF and ZF were estimated to be about 1.81 eV and 2.13 eV from the Tauc-plot (Fig. S4b) by Kubelka-Munk method. Furthermore, the measured flat-band potentials (E_f) of NF and ZF are positioned at 0.13 and -0.3 eV, respectively (Fig. S4c-d). Thus, conduction band (E_{CB}) values of NF and ZF are respectively 0.07 eV and -0.5 eV, and the corresponding valance band (E_{VB}) values of NF and ZF are separately -0.48 and 0.19 eV [23].

To further investigate carrier separation efficiency, the transient photocurrent responses and Electrochemical impedance spectroscopy (EIS) Nyquist plots of NF, ZF and NF@ZF are studied. As Fig. 1h showed, NF@ZF exhibits much higher photocurrent response, which is respectively about 2 and 3 times of NF and ZF, implying that the constructed heterojunction between NF and ZF could inhibit the e^-h^+ pairs

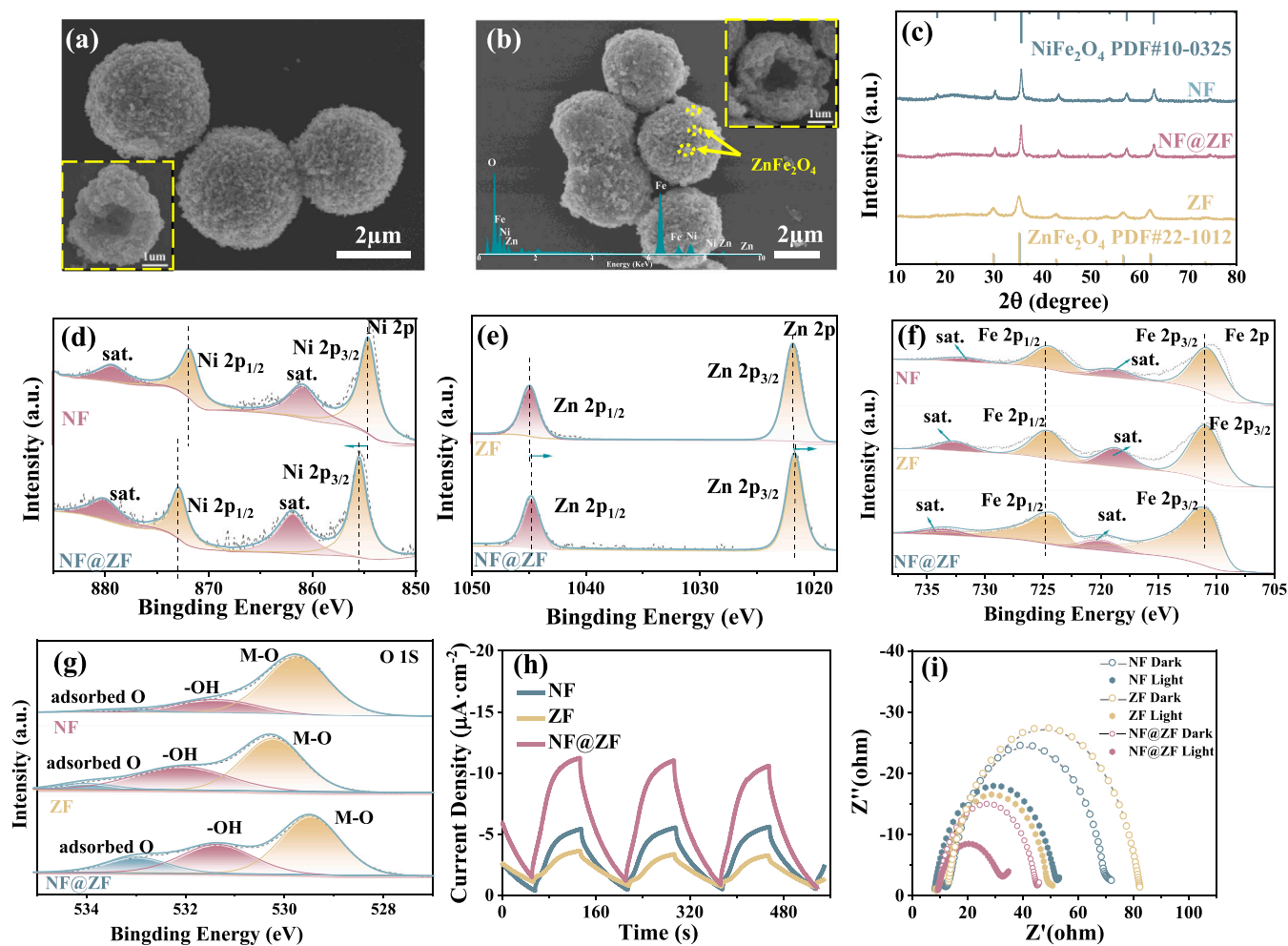


Fig. 1. SEM image of NF (a) and NF@ZF composite (b); XRD patterns of NF@ZF, NF and ZF (c); High-resolution XPS spectra of Ni 2p (d), Zn 2p (e), Fe 2p (f) and O 1s (g); Photocurrent response at 0.4 V bias potential vs. Ag/AgCl. Irradiation conditions were $\lambda > 420$ nm (300 W Xenon lamp fixed at $100 \text{ mW} \cdot \text{cm}^{-2}$ with a cutoff filter). (h); EIS Nyquist plots (i).

recombination and thus enhancing photocurrent response. In addition, NF@ZF shows smaller semicircle compared with NF and ZF (Fig. 1i), revealing that NF@ZF have relatively small diffusion transfer resistance, thus facilitating photoexcited carrier's migration. Under visible light irradiation, the charge transfer was further promoted due to the photoexcitation that resulted in the enhanced PEC activity of the reduced catalyst.

3.2. Characterization of the Janus electrode

Fabrication of Janus electrode is schematically illustrated in Scheme 2. The Janus electrode was studied by SEM and water contact angle to show the hydrophilicity difference of its two sides. Fig. 2a shows the cross-sectional SEM image of the as-obtained Janus electrode. The GF modified by PTFE on the upper part as the hydrophobic side and the NF@ZF catalyst layers on the lower part as the hydrophilic side can be clearly seen. Furthermore, a wettability gradient be created along the direction perpendicular to the Janus film. The PTFE modified side of Janus electrode showed large water contact angle (145.3°) (Fig. 2b, c). The apparently mirror-like gray surface was due to the presence of robust gas film on the hydrophobic layer reflected most of light strongly (Fig. 2d). Because it's hydrophobicity, the ability to gather gas bubbles improved in the prepared Janus electrode, proving the key role of PTFE modification on capturing O_2 rapidly underwater. In contrast, the NF@ZF catalyst layer exhibited hydrophilic property with a water contact angle of 43.0° (Fig. 2e). Also, the dark color of hydrophilic layer showed little light reflection, demonstrating the remarkable wetting of electrolyte into the hydrophilic layer preventing the formation of gas film (Fig. 2f, g). Thus, the Janus electrode showed opposite wettability, with a hydrophilic catalyst layer and a hydrophobic oxygen storage layer.

To compare the ORR activities of the Janus electrodes, HOE and HIE, electrochemical double layer capacitance (C_{dl}) was used to estimate electrolyte contact areas of the electrodes because only sufficient solid/liquid contact could cause adsorption/desorption of ions with cyclic voltammetry (CV) measurement and thus enhance the electrochemical double layer capacitance. As expected, HOE only showed $2.44 \text{ mF}\cdot\text{cm}^{-2}$ (Fig. 3a), less than 5% of that for HIE ($51.32 \text{ mF}\cdot\text{cm}^{-2}$), which illustrated that electrolyte was excluded from the NF@ZF catalysts coated on HOE resulting to few catalyst/liquid contact area and thus limited triple-phase (gas/liquid/gas) interface and negligible current for further reaction. Noted that the C_{dl} of Janus electrode ($23.66 \text{ mF}\cdot\text{cm}^{-2}$) is approximate 1/2 to that of HIE, indicating hydrophobic side as gas storage also occupied 1/2 of the whole Janus electrode, and the remaining hydrophilic portion offered much more solid/liquid interfaces and provided access for NF@ZF to contact electrolyte, leading to strong current response compared with HIE and HOE. The unique opposite wetting properties of the Janus electrode indeed contributed to improve PEC ORR performance. This could be attributed to the synergistic effect of two sides with asymmetrical wettability and uneven PTFE

modification introducing more triple-phase interface.

EIS was determined to explore the influence of hydrophobicity on the diffusion transfer resistance (R_d) of the Janus photocathode. According to Fig. 3b, the R_d values of the Janus electrode and HIE were less than that of HOE. The lower solution resistances of the Janus electrode and HIE were benefit from their rapid ionic/electronic transfer between the hydrophilic electrode surface and the solution.

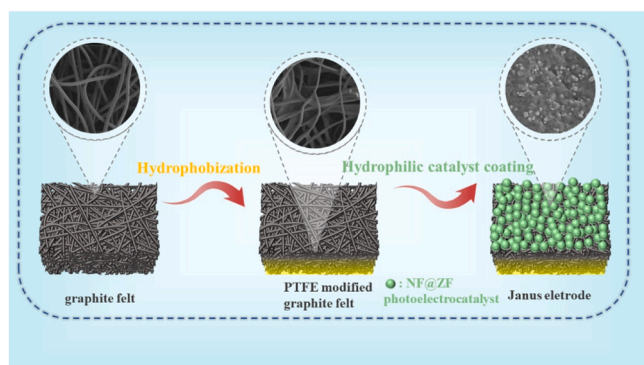
3.3. PEC H_2O_2 production of the Janus photocathode

To investigate the effect of hydrophobicity on the ORR performance, the linear sweep voltammetry (LSV) curves of different electrodes were performed in a three-electrode system. As shown in Fig. 4a, the prepared Janus photocathode exhibited excellent performance with a low onset potential and rapid current density growth, superior over HIE or HOE. Such superior ORR performance of the Janus electrode was attributed to sufficient O_2 supply from hydrophobic gas transport layer and adequate ORR active sites in hydrophilic catalyst layer. However, HIE showed a relatively low current density in LSV curves (only $-4.8 \text{ mA}\cdot\text{cm}^{-2}$ at -1.2 V vs Ag/AgCl). This poor PEC performance occurred because the limited ORR process on HIE, as a result of O_2 mass transfer restriction and low dissolved oxygen concentration in the electrolyte (Fig. 4d). Notably, the dissolved O_2 in electrolyte is the main source for PEC ORR at low overpotential region ($0.4\text{--}0 \text{ V}$ vs. Ag/AgCl), the current density of HOE was lower than that of HIE, demonstrating HOE has limited contact area with the electrolyte (Fig. 4e). Thus, both hydrophilic catalyst layer and hydrophobic gas transport layer in the Janus electrode were important for effective PEC ORR (Fig. 4f).

The effect of electrode potentials on H_2O_2 yields were then investigated by quantitatively monitoring the H_2O_2 concentration after PEC reduction of O_2 for 1 h. As exhibited in Fig. 4b, the H_2O_2 yield reached highest at -0.7 V vs Ag/AgCl. The generation of light-driven H_2O_2 also depended on the pH value of electrolyte, because the process of H_2O_2 generation was a proton-coupled electron transfer process. Excess protons ($\text{pH} = 1.0$) might induce the produced H_2O_2 to be gradually oxidized into H_2O ($H_2O_2 + 2H^+ + 2e^- = 2H_2O$), a less proton-rich environment ($\text{pH} = 5.0$) would lead to a lower H_2O_2 production because of the faster H_2O_2 decomposition. Hence, $\text{pH} = 3$ was the optimum pH value for the catalytic producing H_2O_2 (Fig. S5). The Faraday efficiencies (FEs), energy consumptions (ECs) and H_2O_2 yields were measured to estimate the ORR performance of different electrodes (Fig. 4c). The Janus photocathode with asymmetric wettability generated the largest H_2O_2 yield of $255.9 \text{ mg}\cdot\text{L}^{-1}\cdot\text{h}^{-1}$, compared to those using merely HOE or HIE ($189.5 \text{ mg}\cdot\text{L}^{-1}\cdot\text{h}^{-1}$ on HOE, $84.2 \text{ mg}\cdot\text{L}^{-1}\cdot\text{h}^{-1}$ on HIE). Meanwhile, the Janus photocathode achieved an FE of 72%, much higher than that of 53.2% for HOE and 13.8% for HIE. Normalized EC was evaluated when using the Janus electrode, HIE and HOE, to compare their energy consumptions of H_2O_2 production. Much lower EC of $1.09 \text{ kWh}\cdot\text{kg}^{-1}$ for Janus electrode was obtained, compared with that of $1.51 \text{ kWh}\cdot\text{kg}^{-1}$ for HOE and $5.81 \text{ kWh}\cdot\text{kg}^{-1}$ for HIE. The remarkable ORR performance of Janus electrode was mainly attributed to the integration of a hydrophilic catalyst layer and a hydrophobic gas storage layer (Fig. 4f).

It could be summarized as follows: (1) sufficient and steady O_2 supply from hydrophobic gas storage layer via three-phase contact lines, mitigating dissolved oxygen restriction in the electrolyte; (2) adequate contact area between hydrophilic NF@ZF surface and solution, benefiting ionic/electronic transport in the O_2 reduction process; (3) the created randomly distributed but cross-linked hydrophobic/hydrophilic zones with hydrophilicity gradients induced a large amount of triple-phase interfaces for ORR. (4) Janus electrode allows the fast transport of O_2 , a natural electron scavenger, to the catalytic site, enabling the efficient removal of photogenerated electrons from Z-scheme NF@ZF with strongly coupled interface and inhibit photoexcited carrier's recombination.

To assess the stability of the Janus electrode, the long-term PEC ORR



Scheme 2. Schematic illustration of the Janus electrode fabrication.

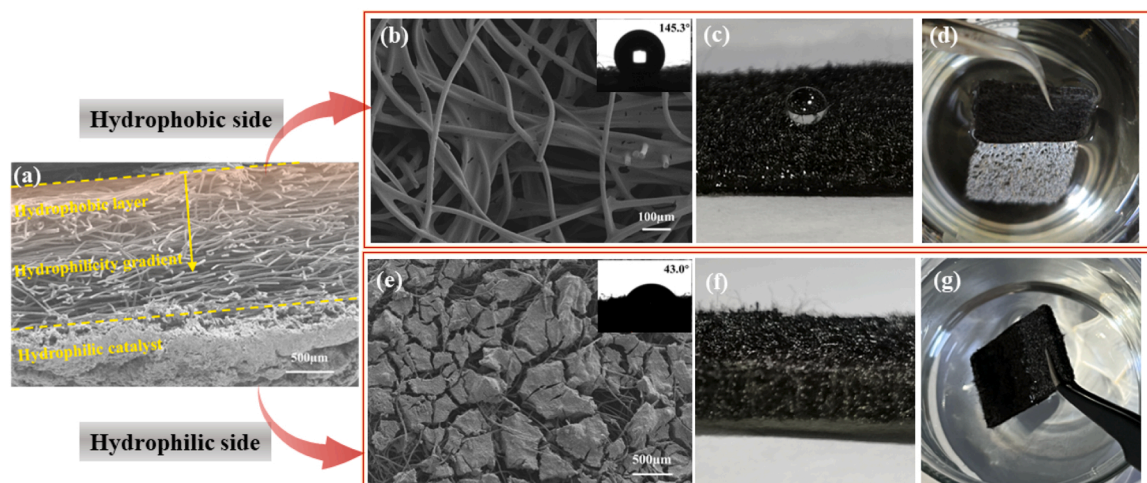


Fig. 2. Cross-sectional SEM images of Janus electrode (a); Hydrophobic (b) and hydrophilic (e) surface SEM images of Janus electrode. Insets are the contact angles of the hydrophobic and hydrophilic surface in Janus electrode; Photograph of hydrophobic gas transport layer (c-d) and hydrophilic catalyst layer (f-g) in Janus electrode.

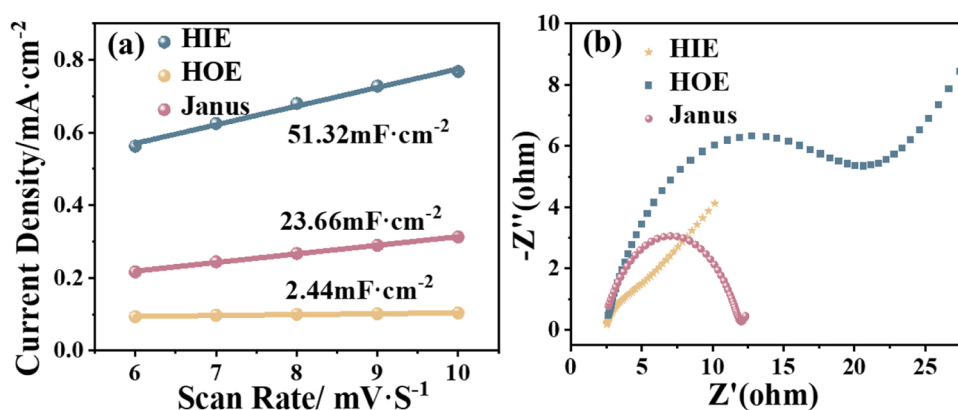


Fig. 3. ECSA measurements (a); EIS Nyquist plots of the Janus electrode, HIE and HOE (b).

reaction was carried out. Fig. 4g shows the *i*-*t* curve almost no current change was observed after 9 h of the test. The concentrations of generated H_2O_2 over time and the corresponding FE were also measured to evaluate the stability performance of the Janus photocathode. As shown in Fig. 4h, the H_2O_2 yield rate exhibited a nearly linear relationship with regards to catalytic duration, and the Faraday efficiency is maintained between 60~80%. Significantly, the generated H_2O_2 was easily decomposed via reacting with photogenerated electrons and holes ($\text{H}_2\text{O}_2 + 2\text{H}^+ + 2\text{e}^- = 2\text{H}_2\text{O}$, $\text{H}_2\text{O}_2 + 2\text{h}^+ = \text{O}_2 + 2\text{H}^+$) during the overall light-driven production of H_2O_2 (Fig. S6) [24,25]. That may be also the reason for low Faradaic efficiency. The XPS and SEM of NF@ZF after long-term testing was characterized (Fig. S7), the inconspicuous change in test results also confirming the outstanding recyclability of the fabricated Janus electrode.

Compared with other literatures, the Janus electrode proposed in this work had an obvious advantage in H_2O_2 yield, current efficiency and energy consumption. As presented in Fig. 4i and Table S1, the comparison suggested that the performance of the constructed NF@ZF Janus electrode is, to a large extent, superior to all other reported Janus electrodes or hydrophobic electrodes [8,20,26–34]. Therefore, the preparation of the novel NF@ZF Janus photocathode through adjusting the hydrophobicity has a remarkable potential as an effective strategy for ORR with an excellent catalytic ability and long stability.

To investigate the pathway of H_2O_2 generation on the prepared NF@ZF catalyst, trapping experiments were conducted during PEC ORR

process (Fig. 5a). There was almost no change in the H_2O_2 generation after adding isopropanol (IPA) or $(\text{NH}_4)_2\text{C}_2\text{O}_4$, implying $\text{OH}\cdot$ and h^+ were not active species during PEC catalysis. However, the production of H_2O_2 was reduced obviously with $\text{K}_2\text{S}_2\text{O}_8$ and 2,2,6,6-Tetramethyl-1-piperidinyloxy (TEMPO), indicating e^- and $\cdot\text{O}_2^-$ was a necessary active group during PEC H_2O_2 generation. The electron transfer number in ORR was tested by rotating disc electrode (RDE), and the LSV of the NF@ZF at increased rotation speeds is shown in Fig. 5b. The Koutecky-Levich (K-L) plots obtained from the LSV curves indicated the numbers of electron transfer (*n*) for ORR on NF@ZF are 1.4 ~ 1.5 (Fig. 5c). The aforementioned results revealed that the production of H_2O_2 was mainly caused by the direct 2e^- ORR ($\text{O}_2 + 2\text{H}^+ + 2\text{e}^- \rightarrow \text{H}_2\text{O}_2$) and indirect 2e^- ORR pathways ($\text{O}_2 + \text{e}^- \rightarrow \cdot\text{O}_2^-$, $\cdot\text{O}_2^- + 2\text{H}^+ + \text{e}^- \rightarrow \text{H}_2\text{O}_2$).

3.4. Janus || Fe in-situ Fenton system for As (III) oxidation and ROX degradation

The oxidation of As (III) to As (V) and the degradation of ROX in the Janus || Fe in-situ Fenton system were investigated (the apparatus used in the experiment is shown in inset of Fig. S8). The potential has a significant influence in increasing efficiency of the oxidation process. It can be seen that the conversion efficiency of As (III) and the degradation efficiency of ROX improved with the rise of potentials, owing to more Fe^{2+} and H_2O_2 can be generated at the higher potential. However, the excess potential might result in the high energy consumption and the

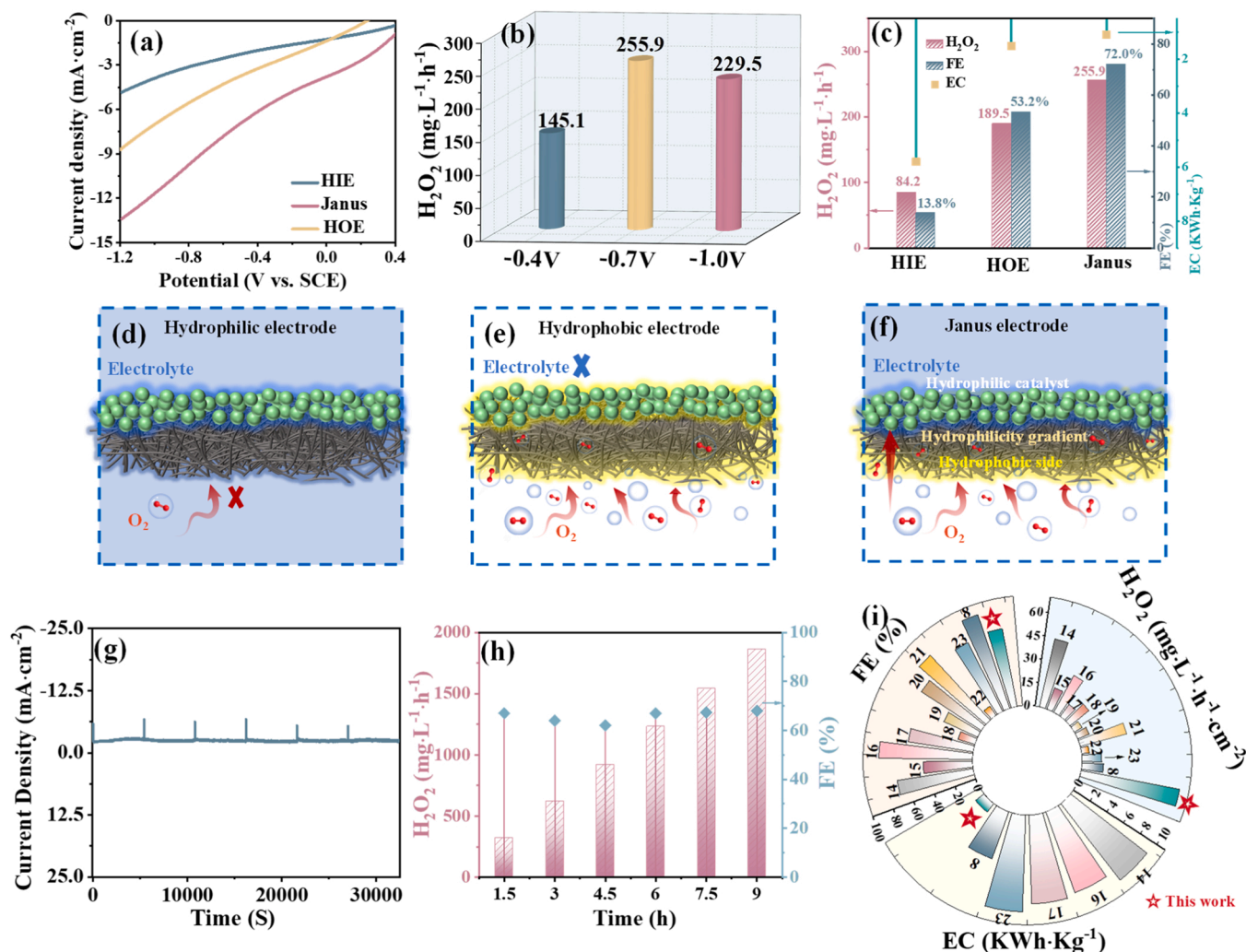


Fig. 4. LSV curves of the Janus electrode, HIE and HOE (a); The effects of applied potential on PEC H_2O_2 production over the Janus electrode (b); H_2O_2 yields and FEs of the Janus electrode, HIE and HOE (c); Schematic illustration of transport and reaction pathways on HIE (d), HOE (e) and the Janus electrode (f) for ORR; Stability experiment for the PEC H_2O_2 production with the Janus electrode (g); H_2O_2 yield and FEs for the Janus electrode at -0.7 V after electrolysis in O_2 -saturated $0.1\text{ M Na}_2\text{SO}_4$ for 9 h. Irradiation conditions were $\lambda > 420\text{ nm}$ (300 W Xenon lamp fixed at $100\text{ mW}\cdot\text{cm}^{-2}$ with a cutoff filter). (h); Comparison with other electrodes for H_2O_2 production (i).

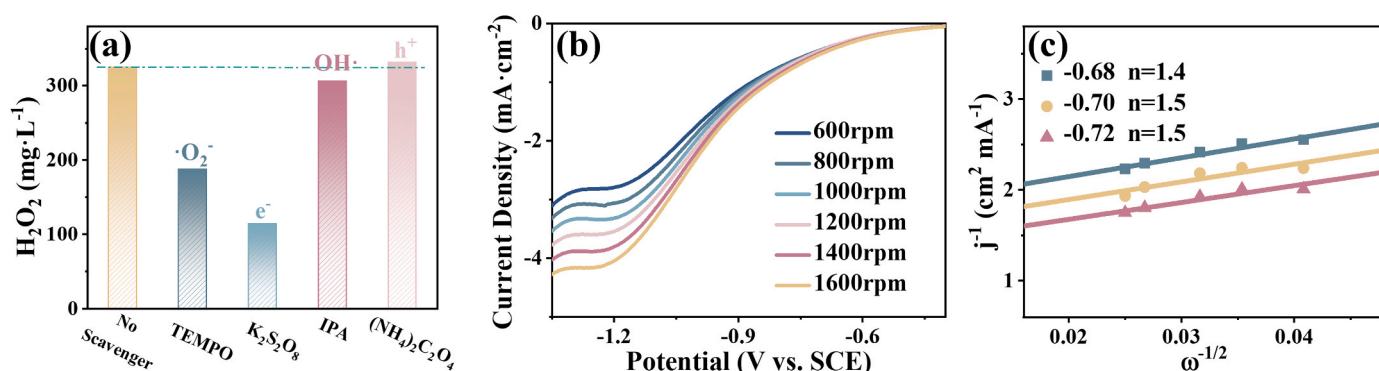


Fig. 5. The effects of various scavengers on the PEC H_2O_2 production (a); LSV of the NF@ZF in O_2 -saturated $0.1\text{ M Na}_2\text{SO}_4$ (pH = 3) at different rotating speed (b); Koutecky-Levich plots of the NF@ZF at the potential range of -0.68 V to -0.72 V (vs. Ag/AgCl) (c).

waste of produced Fe^{2+} . Therefore, the potential of -0.7 V was adequate to the oxidation process (Fig. 6a). The influence of electrolyte pH on the conversion efficiency of As (III) and degradation efficiency of ROX were further investigated by presetting initial pH at 2, 3 and 6,

respectively (Fig. 6a). It was found that low acidic conditions were more beneficial for the oxidation process. The pH-dependent As (III) and ROX oxidation were mainly ascribed to the pH-dependent Fenton reaction between H_2O_2 and Fe^{2+} ions dissolved by anodes. At lower pH values,

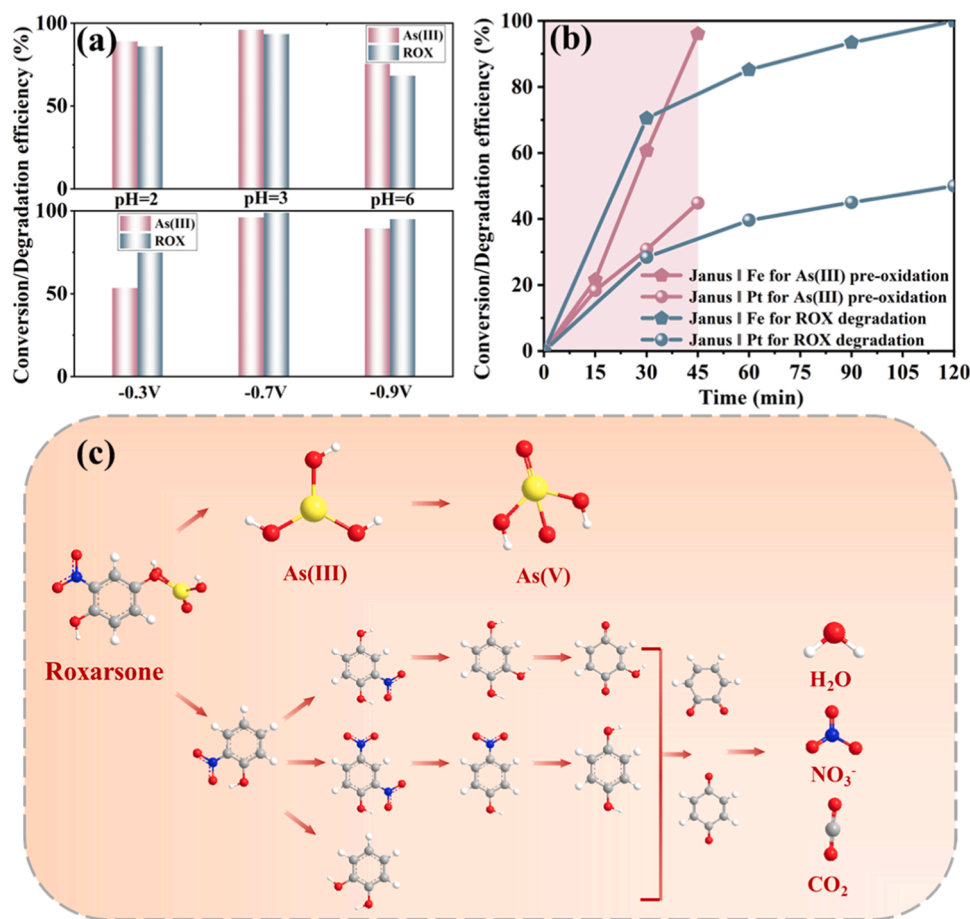


Fig. 6. The effects of applied potential and pH on As (III) oxidation and ROX degradation (a); The As (III) conversion efficiency and ROX degradation efficiency of Janus || Fe in-situ Fenton system and Janus || Pt system (b); The proposed ROX degradation pathway in the Janus || Fe in-situ Fenton system (c).

H₂O₂ could strongly interact with Fe²⁺ to form •OH with strong oxidizing potential, which was beneficial for the fast ROX degradation and As (III) oxidation processes. Due to masses of OH⁻ in higher pH electrolyte, they were easy to react with Fe³⁺ to form precipitated iron oxides on electrode surface, which set huge barriers to the activation of H₂O₂, resulting in the lower •OH generation. Therefore, pH = 3 was chosen as the initial pH of the system in subsequent experiments.

The oxidation properties of the PEC system were evaluated by using different anodes. The conversion or degradation efficiency of different PEC systems for As (III) and ROX were shown in Fig. 6b. The Janus || Fe in-situ Fenton system exhibited more prominent catalytic performance than Janus || Pt system, in which the degradation efficiency of ROX reaches to about 100% within 120 min and 20 ppm As (III) were almost totally oxidized into As (V) within 45 min (44.8% for As (III) within 45 min and 50.1% for ROX within 120 min in Janus || Pt system). The corresponding kinetic behaviors of As (III) and ROX oxidation in different PEC systems were presented in Fig. S9. It was obvious that the oxidation property was enhanced by in situ Fenton reaction. Subsequently, the degradation pathways for ROX were investigated by Mass spectrometry (MS) measurements (Fig. 6c). Firstly, the As-C bond of ROX was attacked by HO•, leading to the formation of o-nitrophenol and As (III). As (III) is rapidly oxidized to As (V), while o-nitrophenol is further converted to other organic intermediates, and can be ultimately mineralized to NO₃⁻, CO₂, and H₂O under the conditions of adequate oxidation time [35].

The attention of most researchers was only paid to the preoxidation of As (III) or the degradation of the ROX pollutants in the treatment of arsenic contamination by PEC processes. However, immobilization of the less toxic As (V) released from the oxidation process can be even

more critical for the overall performance of the treatment approach. Fortunately, the Fe (III) (hydro)oxides formed from hydrolysis of the Fe³⁺ generated from the Fenton reaction could take critical part in the sorptive removal of inorganic arsenic species. At the end of electrolysis, the pH of the treated electrolyte was adjusted to 9 and the orange precipitate was observed, consistent with Fe (III) (hydro)oxides (Fig. 7a). After standing the solution for 24 h, measurements of total arsenic in supernatant indicated that more than 93% of arsenic has been removed (Fig. 7b). Through forming stable inner sphere complex with arsenate [36], the inorganic arsenic species in solution can effectively remove through Fe (III) (hydro)oxides adsorption. The precipitates were collected and investigated by XPS. As shown in Fig. 7c, two distinct peaks centered at 724.7 and 711.4 eV on the Fe 2p spectra, indicating that the Fe element mainly exists in the Fe³⁺ ions. The peak at 45.6 eV was assigned to As 3d of As (V) (Fig. 7d), arsenic present in the form of As (V) in the precipitate suggests that most of As (III) was indeed oxidized through the Janus || Fe in-situ Fenton system.

Typically, the charge transfer at the interfacial phase may follow the type II or Z-scheme transfer mechanism. •O₂⁻ is observed in the PEC ORR system (Fig. 5a), demonstrating that the photoexcited e⁻ accumulate on the CB (-0.50 V vs. NHE) of ZF rather than the CB (-0.07 V vs. NHE) of NF. The results fully reveal the Z-type charge transfer pathway in NF@ZF. XPS spectra were also used to probe the photoexcited carrier migration route (Fig. 1d, e). The binding energy of Zn 2p in NF@ZF negatively shifted compared to ZF and Ni 2p positively shifted of compared to NF, implying the photoexcited e⁻ were moved from NF to ZF in accordance with a direct Z-scheme charge transfer mechanism. Furthermore, the M-S plot of NF@ZF (Fig. S10) exhibited a stationary region in the midsection. This feature indicating a high density

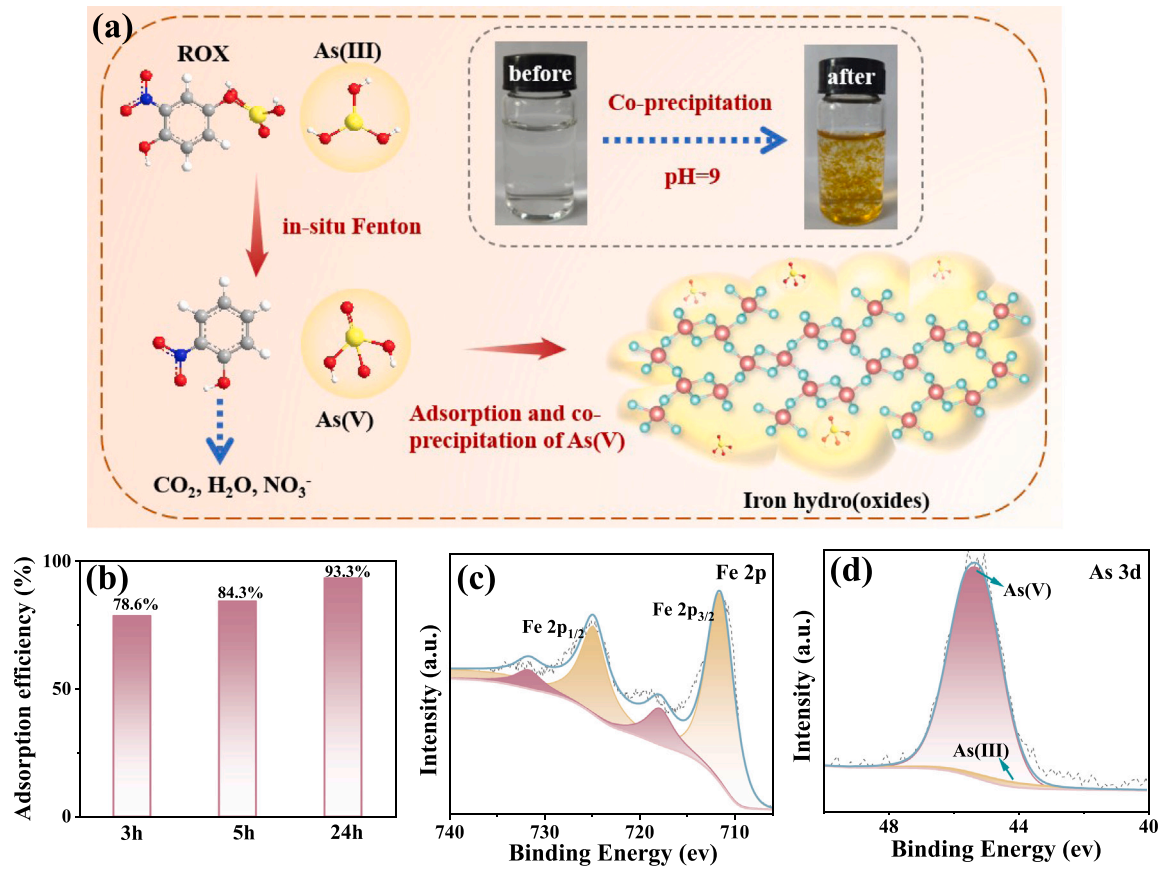
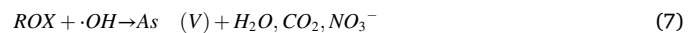
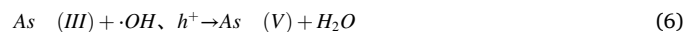
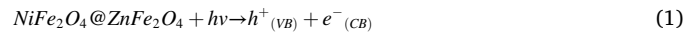


Fig. 7. Schematic illustration of Fe (III) (hydro) oxides adsorption (a); adsorption cure of As (V) by Fe (III) (hydro) oxides (b); Fe 2p (d) and As 3d (e) core level photoelectron spectra of the precipitate.

monoenergetic interface states located at the NF@ZF heterojunction, indicating that Z-scheme heterojunction could form [25]. The Z-scheme heterostructure not only facilitates an effective spatial separation of photo-induced e^-h^+ pairs but also enhances the redox ability of the photocatalyst caused by an increase in redox potential. Based on the above analysis, the charge-transfer mechanism of H₂O₂ generation over NF@ZF heterojunction was proposed in Fig. 8. Ultimately, we have developed the Janus electrode based on air-liquid-solid reaction interface for the rapid and continuous delivery of electron scavenger oxygen (-0.33 V vs. NHE). Photogenerated e^-h^+ pairs are efficiently separated, resulting in significantly enhanced Z-scheme NF@ZF heterojunction kinetics reaction rate to realize a high yield of H₂O₂.

The As (III) oxidation mechanism of the Janus || Fe in-situ Fenton system was also be investigated. The result of the free radical trapping

experiments is shown in Fig. S11, the addition of IPA significantly inhibited As (III) oxidation, implying high concentration of $\cdot OH$ generated from the enhanced decomposition of H₂O₂ by Fe (II) (Fig. 9). Meanwhile, $\bullet O_2^-$ also play an important role in As (III) oxidation, that can be attributed to the capture of the O₂ reduction intermediate ($\bullet O_2^-$) by TEMPO. Besides, direct oxidation by holes made up a very small percentage in the As (III) oxidation process. Based on the above analysis, the possible reaction equations could be proposed as Eqs. (1)–(7):



4. Conclusion

In conclusion, we designed a 3D porous GF-based Janus solar-powered photoelectrode with asymmetric wettability, employing a PTFE thin layer coated on one side and 3D hollow sphere NF@ZF Z-scheme heterojunction photocatalysts coated on the other side for fast and stable PEC in situ H₂O₂ generation. The NF@ZF catalyst was demonstrated effective in selective generation of H₂O₂ from photoelectrochemical 2e⁻ ORR, and the Janus photo-electrode exhibited superior H₂O₂ generation performance of 255.9 mg·L⁻¹·h⁻¹, superior

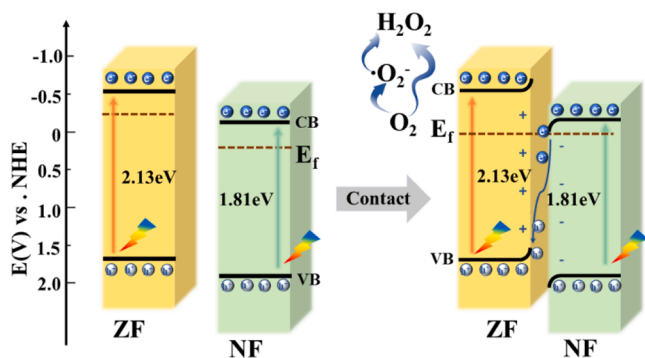


Fig. 8. Energy band diagrams and photoelectrocatalytic mechanism of NF@ZF heterojunction.

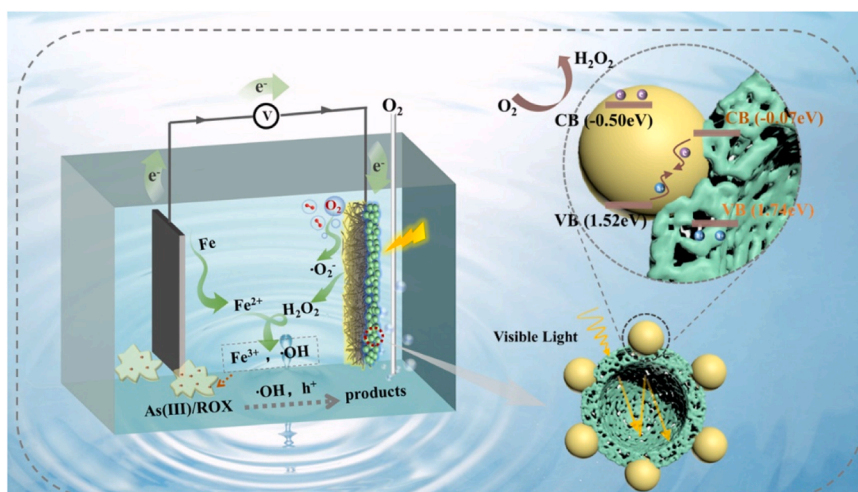


Fig. 9. Mechanism diagram of the PEC process.

over HOE and HIE electrodes. By applying the Janus photo-cathodic H_2O_2 generation system coupled with Fe sacrifice anode, the self-constructed PEC in-situ Fenton system achieve an excellent As (III) oxidation efficiency of 96.1% within 45 min and a superior degradation efficiency toward of roxarsone more than 99% within 120 min. In addition, the Fe (III) (hydro)oxide precipitate formed from iron corrosion effectively captured the inorganic arsenic released for the complete removal of arsenic. The concept and principles in this work should be applicable for designing photoelectrochemical H_2O_2 production electrodes and removing pollutants on a large scale in the future.

CRediT authorship contribution statement

Yan Sun: Conceptualization, Methodology, Validation, Formal analysis, Investigation, Data curation, Writing – original draft, Writing – review & editing, Visualization. **Lei Zhang:** Conceptualization, Resources, Supervision, Project administration, Funding acquisition.

Declaration of Competing Interest

The authors declare that they have no known competing financial interests or personal relationships that could have appeared to influence the work reported in this paper.

Data availability

Data will be made available on request.

Acknowledgments

This project was supported by the National Natural Science Foundation of China (NSFC 52072164) and (NSFC 52102104), Doctoral Start-up Foundation of Liaoning Province (2021-BS-089). The authors also thank their colleagues and other students who participated in this study. The authors would like to thank Jilong Gao from Shiyanjia Lab (www.shiyanjia.com) for support of MS analysis and XRD analysis.

Appendix A. Supporting information

Supplementary data associated with this article can be found in the online version at [doi:10.1016/j.apcatb.2023.123549](https://doi.org/10.1016/j.apcatb.2023.123549).

References

- [1] Gh Moon, S. Kim, Y.J. Cho, J. Lim, Dh Kim, W. Choi, Synergistic combination of bandgap-modified carbon nitride and WO_3 for visible light-induced oxidation of arsenite accelerated by in-situ Fenton reaction, *Appl. Catal. B* 218 (2017) 819–824, <https://doi.org/10.1016/j.apcatb.2017.07.021>.
- [2] N. Chen, Y. Wan, G. Zhan, X. Wang, M. Li, L. Zhang, Simulated solar light driven roxarsone degradation and arsenic immobilization with hematite and oxalate, *Chem. Eng. J.* 384 (2020), 123254, <https://doi.org/10.1016/j.cej.2019.123254>.
- [3] P. Wang, T. Hayashi, Q. Meng, Q. Wang, H. Liu, K. Hashimoto, L. Jiang, Highly boosted oxygen reduction reaction activity by tuning the underwater wetting state of the superhydrophobic electrode, *Small* 13 (2017), 1601250, <https://doi.org/10.1002/sml.201601250>.
- [4] X. Wei, M. Pu, Y. Jin, M. Wessling, Efficient Electrocatalytic N_2 Reduction on Three-Phase Interface Coupled in a Three-Compartment Flow Reactor for the Ambient NH_3 Synthesis, *ACS Appl. Mater. Interfaces* 13 (2021) 21411–21425, <https://doi.org/10.1021/acsami.1c03698>.
- [5] N.T. Nesbitt, T. Burdyny, H. Simonson, D. Salvatore, D. Bohra, R. Kas, W.A. Smith, Liquid-Solid Boundaries Dominate Activity of CO_2 Reduction on Gas-Diffusion Electrodes, *ACS Catal.* 10 (2020) 14093–14106, <https://doi.org/10.1021/acscatal.0c03319>.
- [6] Q. Zhang, M. Zhou, G. Ren, Y. Li, Y. Li, X. Du, Highly efficient electrosynthesis of hydrogen peroxide on a superhydrophobic three-phase interface by natural air diffusion, *Nat. Commun.* 11 (2020), 1731, <https://doi.org/10.1038/s41467-020-15597-y>.
- [7] Y. Li, H. Zhang, N. Han, Y. Kuang, J. Liu, W. Liu, H. Duan, X. Sun, Janus electrode with simultaneous management on gas and liquid transport for boosting oxygen reduction reaction, *Nano Res* 12 (2018) 177–182, <https://doi.org/10.1007/s12274-018-2199-1>.
- [8] H. Zhang, Y. Zhao, Y. Li, G. Li, J. Li, F. Zhang, Janus Electrode of Asymmetric Wettability for H_2O_2 Production with Highly Efficient O_2 Utilization, *ACS Appl. Energy Mater.* 3 (2019) 705–714, <https://doi.org/10.1021/acsaem.9b01908>.
- [9] L. Yang, H. Yu, Y. Wu, L. Zhang, Assembled 3D MOF on 2D Nanosheets for Self-boosting Catalytic Synthesis of N-doped Carbon Nanotube Encapsulated Metallic Co Electrocatalysts for Overall Water Splitting, *Appl. Catal. B* 271 (2020), 118939, <https://doi.org/10.1016/j.apcatb.2020.118939>.
- [10] S. Huang, Y. Xu, T. Zhou, M. Xie, Y. Ma, Q. Liu, L. Jing, H. Xu, H. Li, Constructing magnetic catalysts with in-situ solid-liquid interfacial photo-Fenton-like reaction over $\text{Ag}_3\text{PO}_4/\text{NiFe}_2\text{O}_4$ composites, *Appl. Catal. B* 225 (2018) 40–50, <https://doi.org/10.1016/j.apcatb.2017.11.045>.
- [11] X. Rong, H. Chen, J. Rong, X. Zhang, J. Wei, S. Liu, X. Zhou, J. Xu, F. Qiu, Z. Wu, An all-solid-state Z-scheme $\text{TiO}_2/\text{ZnFe}_2\text{O}_4$ photocatalytic system for the N_2 photofixation enhancement, *Chem. Eng. J.* 371 (2019) 286–293, <https://doi.org/10.1016/j.cej.2019.04.052>.
- [12] J. Zheng, L. Zhang, Incorporation of CoO nanoparticles in 3D marigold flower-like hierarchical architecture MnCo_2O_4 for highly boosting solar light photo-oxidation and reduction ability, *Appl. Catal. B* 237 (2018) 1–8, <https://doi.org/10.1016/j.apcatb.2018.05.060>.
- [13] X. Chen, J. Wang, Y. Chai, Z. Zhang, Y. Zhu, Efficient photocatalytic overall water splitting induced by the giant internal electric field of a g- C_3N_4 /rGO/PDIP Z-scheme heterojunction, *Adv. Mater.* 33 (2021), 2007479, <https://doi.org/10.1002/adma.202007479>.
- [14] J. Zheng, L. Zhang, Designing 3D Magnetic Peony Flower-like Cobalt Oxides/g- C_3N_4 Dual Z-Scheme Photocatalyst for Remarkably Enhanced Sunlight Driven Photocatalytic Redox Activity, *Chem. Eng. J.* 369 (2019) 947–956, <https://doi.org/10.1016/j.cej.2019.03.131>.
- [15] Q. Zhang, L. Jiang, J. Wang, Y. Zhu, Y. Pu, W. Dai, Photocatalytic degradation of tetracycline antibiotics using three-dimensional network structure perylene

- diimide supramolecular organic photocatalyst under visible-light irradiation, *Appl. Catal. B* 277 (2020), 119122, <https://doi.org/10.1016/j.apcatb.2020.119122>.
- [16] X. Zhang, J. Wang, B. Xiao, Y. Pu, Y. Yang, J. Geng, D. Wang, X. Chen, Y. Wei, K. Xiong, Y. Zhu, Resin-based photo-self-Fenton system with intensive mineralization by the synergistic effect of holes and hydroxyl radicals, *Appl. Catal. B* 315 (2022), 121525, <https://doi.org/10.1016/j.apcatb.2022.121525>.
- [17] L. Yang, G. Sun, H. Fu, L. Zhang, Isolation of cobalt single atoms on hollow B, N co-doped defective carbon nanotubes for hydrogen peroxide production and tandem reagent-free electro-Fenton oxidation, *Chem. Eng. J.* 472 (2023), 145052, <https://doi.org/10.1016/j.cej.2023.145052>.
- [18] K. Holst-Olesen, M. Reda, H.A. Hansen, T. Vegge, M. Arenz, Enhanced oxygen reduction activity by selective anion adsorption on non-precious-metal catalysts, *ACS Catal.* 8 (2018) 7104–7112, <https://doi.org/10.1021/acscatal.8b01584>.
- [19] J.A. Zamora Zeledón, G.A. Kamat, G.T.K.K. Gunasooriya, J.K. Nørskov, M. B. Stevens, T.F. Jaramillo, Probing the effects of acid electrolyte anions on electrocatalyst activity and selectivity for the oxygen reduction reaction, *ChemElectroChem* 8 (2021) 2467–2478, <https://doi.org/10.1002/celec.202100500>.
- [20] X. Yu, M. Zhou, G. Ren, L. Ma, A novel dual gas diffusion electrodes system for efficient hydrogen peroxide generation used in electro-Fenton, *Chem. Eng. J.* 263 (2015) 92–100, <https://doi.org/10.1016/j.cej.2014.11.053>.
- [21] Y. Xiong, Q. Tong, W. Shan, Z. Xing, Y. Wang, S. Wen, Z. Lou, Arsenic transformation and adsorption by iron hydroxide/manganese dioxide doped straw activated carbon, *Appl. Surf. Sci.* 416 (2017) 618–627, <https://doi.org/10.1016/j.apsusc.2017.04.145>.
- [22] V. Lenoble, Arsenite oxidation and arsenate determination by the molybdenum blue method, *Talanta* 61 (2003) 267–276, [https://doi.org/10.1016/s0039-9140\(03\)00274-1](https://doi.org/10.1016/s0039-9140(03)00274-1).
- [23] X. Liu, D. Xu, D. Zhang, G. Zhang, L. Zhang, Superior performance of 3 D Co-Ni bimetallic oxides for catalytic degradation of organic dye: Investigation on the effect of catalyst morphology and catalytic mechanism, *Appl. Catal. B* 186 (2016) 193–203, <https://doi.org/10.1016/j.apcatb.2016.01.005>.
- [24] J. Cai, J. Huang, S. Wang, J. Iocozzia, Z. Sun, J. Sun, Y. Yang, Y. Lai, Z. Lin, Crafting mussel-inspired metal nanoparticle-decorated ultrathin graphitic carbon nitride for the degradation of chemical pollutants and production of chemical resources, *Adv. Mater.* 31 (2019), 1806314, <https://doi.org/10.1002/adma.201806314>.
- [25] L. Yang, J. Wang, T. Ma, L. Zhang, Nanointerface engineering Z-scheme CuBiOS@CuBi₂O₄ heterojunction with O-S interpenetration for enhancing photocatalytic hydrogen peroxide generation and accelerating chromium (VI) reduction, *J. Colloid Interface Sci.* 611 (2022) 760–770, <https://doi.org/10.1016/j.jcis.2021.11.100>.
- [26] Y. Zheng, J. He, S. Qiu, D. Yu, Y. Zhu, H. Pang, J. Zhang, Boosting hydrogen peroxide accumulation by a novel air-breathing gas diffusion electrode in electro-Fenton system, *Appl. Catal. B* 316 (2022), 121617, <https://doi.org/10.1016/j.apcatb.2022.121617>.
- [27] H. He, B. Jiang, J. Yuan, Y. Liu, X. Bi, S. Xin, A novel dual gas diffusion electrodes of H₂O₂ utilizing HNO₃ modified graphite/polytetrafluoroethylene cathode with exterior hydrophobic film, *J. Colloid Interface Sci.* 533 (2019) 471–480, <https://doi.org/10.1016/j.jcis.2018.08.092>.
- [28] F. Yu, Y. Wang, H. Ma, Enhancing the yield of H₂O₂ from oxygen reduction reaction performance by hierarchically porous carbon modified active carbon fiber as an effective cathode used in electro-Fenton, *J. Environ. Chem. Eng.* 838 (2019) 57–65, <https://doi.org/10.1016/j.jelechem.2019.02.036>.
- [29] W. Zhou, X. Meng, J. Gao, F. Sun, G. Zhao, Janus graphite felt cathode dramatically enhance the H₂O₂ yield from O₂ electroreduction by the hydrophilicity-hydrophobicity regulation, *Chemosphere* 278 (2021), 130382, <https://doi.org/10.1016/j.chemosphere.2021.130382>.
- [30] Y. Zhang, L. Lin, D. Jia, L. Dong, X. Pan, M. Liu, H. Huang, Y. Hu, J.C. Crittenden, Inactivation of *Microcystis aeruginosa* by H₂O₂ generated from a carbon black polytetrafluoroethylene gas diffusion electrode in electrolysis by low-amperage electric current, *Environ. Pollut.* 324 (2023), 121316, <https://doi.org/10.1016/j.envpol.2023.121316>.
- [31] Z. Chen, H. Dong, H. Yu, H. Yu, In-situ electrochemical flue gas desulfurization via carbon black-based gas diffusion electrodes: Performance, kinetics and mechanism, *Chem. Eng. J.* 307 (2017) 553–561, <https://doi.org/10.1016/j.cej.2016.08.116>.
- [32] J. Hou, Z. Xu, J. Ji, Y. Zhao, M. Gao, C. Jin, Enhanced in-situ electro-generation of H₂O₂ using PTFE and NH₄HCO₃ modified C/PTFE electrode for treatment of landfill leachate, *J. Environ. Manag.* 295 (2021), 112933, <https://doi.org/10.1016/j.jenvman.2021.112933>.
- [33] M. Li, X. Qin, M. Gao, T. Li, Y. Lv, Graphitic carbon nitride and carbon nanotubes modified active carbon fiber cathode with enhanced H₂O₂ production and recycle of Fe³⁺/Fe²⁺ for electro-Fenton treatment of landfill leachate concentrate, *Environ. Sci. Nano.* 9 (2022) 632–652, <https://doi.org/10.1039/d1en01095f>.
- [34] X. Sun, J. Lv, Z. Yan, Z. Sun, A three-dimensional gas diffusion electrode without external aeration for producing H₂O₂ and eliminating amoxicillin using electro-Fenton process, *J. Environ. Chem. Eng.* 10 (2022), <https://doi.org/10.1016/j.jece.2022.107301>.
- [35] X. Li, J. He, J. Lu, Y. Zhou, Y. Zhou, In-situ production and activation of H₂O₂ for enhanced degradation of roxarsone by FeS₂ decorated resorcinol-formaldehyde resins, *J. Hazard. Mater.* 424 (2022), 127650, <https://doi.org/10.1016/j.jhazmat.2021.127650>.
- [36] M. Chen, H. Hu, M. Chen, C. Wang, Q. Wang, C. Zeng, Q. Shi, W. Song, X. Li, Q. Zhang, In-situ production of iron flocculation and reactive oxygen species by electrochemically decomposing siderite: An innovative Fe-EC route to remove trivalent arsenic, *J. Hazard. Mater.* 441 (2023), 129884, <https://doi.org/10.1016/j.jhazmat.2022.129884>.